Bachelor's Thesis

Der Einfluss von Rühren und zeitabhängigem Antrieb auf die Ausbildung von Niederschlag

The Influence of Stirring and Time-Dependent Driving on the Formation of Precipitation

prepared by

Julian Vogel

from Herford

at the Max Planck Institute for Dynamics and Self-Organization
and the Georg-August-Universität Göttingen

Preface

This thesis would not have been possible without the help of others. First of all, I would like to thank my supervisor Jürgen Vollmer who provided helpful advice throughout my thesis. I very much enjoyed the insightful discussions about physics and other topics.

Special thanks go to Martin Rohloff for supervision in laboratory work. I benefitted from his support in performing the stirring measurements and modifying the LabVIEW code.

Darcy Jacobson who joined the research group within the scope of a RISE summer internship assisted me in collecting and analysing data for the time-dependent heating. I am grateful for the fruitful collaboration.

I would like to thank Artur Wachtel for performing "magic" on my computer, whenever it was necessary.

During my time at the institute I had the pleasure of being in good company thanks to everyone from Jürgen's and Marco's group.

Contents

Contents

List of Figures

1 Introduction

1.1 Motivation

Formation of clouds and rain, yet an everyday phenomenon, is governed by complex processes on the microscale that are not completely understood. Performing measurements in real clouds is, however, a difficult task. Fortunately, demixing of binary fluids strongly resembles the formation of rain droplets in so called *warm clouds*[1]. Consider an uprising air parcel in the atmosphere that contains water vapour. It expands as pressure releases, and adiabatic cooling leads to condensation of rain droplets. Similar to cloud formation in the atmosphere, condensation of droplets in a binary fluid is induced by changes in temperature. Therefore it can be used as a model system to study precipitation in the laboratory under well controlled conditions.

Until now, experiments have focussed on a constant thermodynamic driving, i. e. temperature ramps where the volume flux onto the droplets is kept constant [2, 4, 8, 9, 15]. By this means it was possible to derive a prediction for the time interval of precipitation [8]. Despite its benefits this approach captures conditions in real clouds only to some extent. In particular, two important aspects in atmospheric clouds were not covered: the effect of flow and of fluctuations of the ramp rate due to turbulence on different length scales [14, p. 253].

In this thesis I will present experimental results on precipitation in a binary mixture of iso-butoxyethanol and water. Two different approaches were used to explore the effects of turbulence. First, we performed experiments where the sample was moderately stirred during phase separation. In another series of measurements a time-dependent driving of the system was used. The idea behind this was to model overturns in an uprising parcel of air. A constant thermodynamic driving

---

[1]In warm clouds the temperature is always so high that ice particles need not to be taken into account to describe droplet growth. In contrast, at mid latitudes one typically encounters cold clouds where freezing of droplets and ice play an essential role for the dynamics of rain initiation (see [7, pp. 94-95]).

corresponds to air that is monotonically carried upwards. In clouds we assume to have circulations [7]. We assessed their effect by superimposing the ramp rate with oscillations on a smaller time scale than the precipitation period.

1.2 Schematic View on Oscillatory Phase Separation

In this section I will sketch the dynamics of phase separation in binary systems. The principles I discuss here are universal and apply for binary fluids as well as for clouds in the atmosphere. The processes can be illustrated with the help of a phase diagram like the one in Fig. 1.1. It illustrates the qualitative behaviour of a two component mixture depending on temperature T and composition ϕ. The composition ϕ can be either volume or mass fraction of one of the components. In this example a phase diagram with an upper critical point is shown, which means that the phases will separate when the system is cooled (which is the case of rain droplets precipitating in air). The opposite case which is less common applies to the mixture used in our experiments: It has a lower critical point and thus demixes upon heating.

The curve in the diagram is the coexistence curve (binodal). For values of T and ϕ that are above the curve the system is miscible. On the contrary it will demix into two separate phases in the region below the coexistence curve (also referred to as miscibility gap). The equilibrium compositions of the two phases are then those of the left (ϕ_l) and the right (ϕ_r) branch on the binodal for a given temperature T_1.

Now consider the system being within the miscibility gap with two macroscopic phases in equilibrium. For moderate temperature changes the dynamics of phase separation can be descibed as follows:
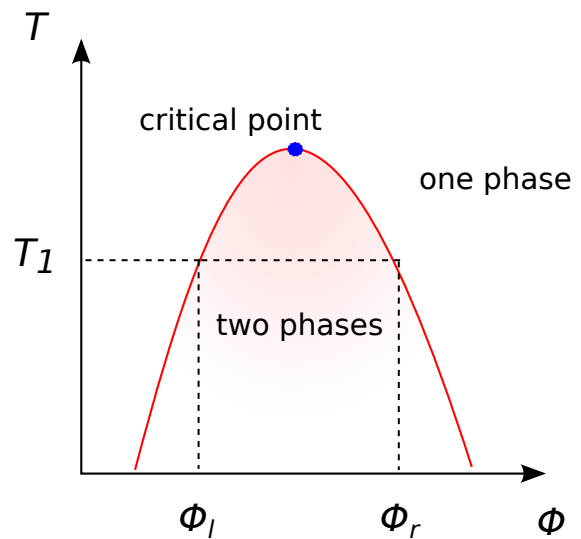
Figure 1.1: Schematic phase diagram for a binary mixture with upper critical point.

1. The system first enters a state of supersaturation: even though the temperature has been changed the composition of the phases does not change considerably because diffusion is not fast enough on the length scales of the macroscopic

domain size of the system. The mismatch between the observed composition and the thermodynamic equilibrium composition is called supersaturation.

2. For large supersaturation droplets of the one phase nucleate within the other, hence relaxing the supersaturation.

3. Next, the supersaturation is further decreased by diffusion towards droplets. It is a fast process now due to the dramatically reduced distance to the next phase boundary.

4. When the droplets grow bigger they start to feel gravity and sediment in the direction of the interface between the layers. The growth is then dominated by coalescence with other droplets at the price of a decrease in droplet number and a growing diffusion path. Thus supersaturation can not be relaxed effectively.

In the end all droplets are removed and the composition of the system can again not keep pace with ramp. When the temperature is slowly ramped the cycle is repeated. This leads to oscillations in the precipitation (see Fig. 1.2).

Figure 1.2: Schematic cycle of precipitation.

1.3 Basics of Synchronization

We model overturns in uprising clouds by oscillations in the heating rate. Since we also expect oscillations in the precipitation we consider the theoretical basics of a

weakly forced oscillator. A detailed description can be found in [11, pp. 49-53, 65-66]. Here, a summery of the main concepts that are relevant for our case is given.
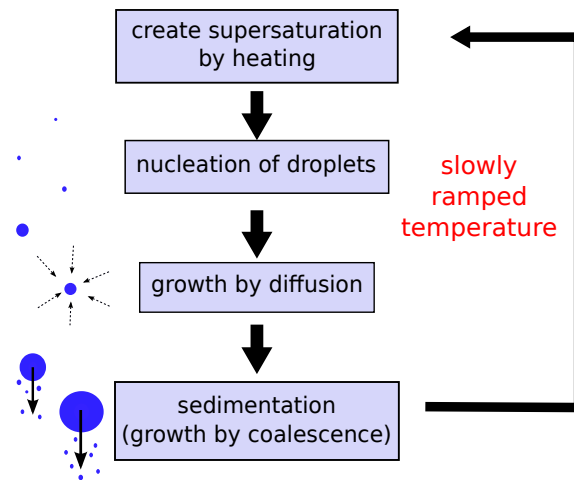
Let us denote the frequency of the undisturbed oscillator by ω_0, which corresponds to the frequency of the precipitation cycle in Fig. 1.2 The external force on the oscillator also is periodic and characterized by its frequency ω (in our case the frequency of cloud convection) and its amplitude A. For a fixed amplitude one finds that up to a certain mismatch in frequencies ω and ω_o the oscillator is synchronized with the external force, i. e. the observed frequency of the oscillator Ω equals the driving frequency ω. For a smaller amplitude synchronization is only possible when the difference of ω and ω_0 is smaller. The synchronization region within the (ω, A) plane is called *Arnold tongue.* For synchronized oscillations a constant phase shift between the external force and the driven oscillator is observed. For this reason one also speaks of *phase locking.*

In general the frequency of the driven oscillator Ω does not necessarily have to be equal to ω. One can, for example, easily imagine a synchronized state where two periods of the driven oscillator lie within one period of the driving force. This would be a synchronization of the order 2:1 ($2\omega = 1\Omega$). In general synchronization can be found for any order $n : m$, where n and m are integer, and the frequencies fulfill $n\omega = m\Omega$. This gives rise to a large amount of Arnold tongues that are schematically drawn in Fig. 1.3. Typically the 1:1 synchronization is dominant and Arnold tongues of higher orders are narrower. The actual shapes of the Arnold tongues depend on the form of the driving force.
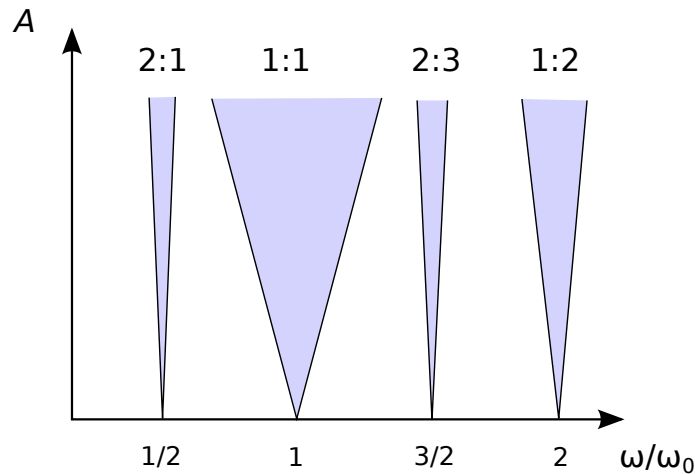
Figure 1.3: Sketch of Arnold tongues in the plane defined by driving frequency ω and driving amplitude A. Reproduced from [11].

1.4 Outline

This thesis is organized as follows: In chapter 2 I present the model system that we use to study oscillatory phase separation. It is recapitulated how a constant thermodynamic driving is achieved and a prediction for the oscillation period is derived. On the basis of this temperature ramps for an oscillatory driving are designed. Chapter 3 adresses the experimental techniques. The setup is described as well as the experimental procedure. Also, space-time plots are introduced as an important method of data analysis. In the subsequent chapters I present the experimental results. Chapter 4 focusses on the stirring experiments, while the experiments with a time-dependent driving are analyzed in chapter 5. The thesis ends with conclusions in chapter 6.

2 The Model System

Previous experiments on oscillations in binary demixing have been carried out with different systems such as microemulsions [19], polymer solutions [2], mixtures of methanol and hexane [2] and water and 2-butoxyethanol [20]. I study demixing in a system of iso-butoxyethanol (i-BE) and water which has previously been used in experiments by Tobias Lapp and Martin Rohloff [8, 9, 15].

2.1 Properties of the System
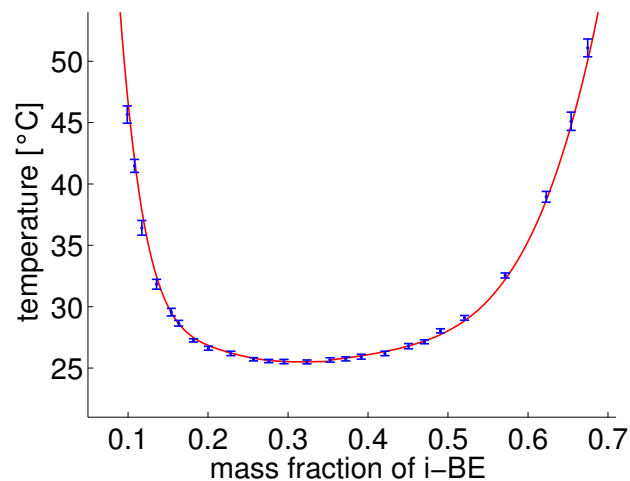
Figure 2.1: Phase diagram of the iso-butoxyethanol/water system showing the co-existence curve. The system demixes in the region above the curve. Measured datapoints (blue) and polynomial fit (red). Reprinted from [15].

A special feature of the iso-butoxyethanol-water system is a lower critical point at about $T_c = 25\,°C$ and mass fraction $\phi_c = 0.3$ of iso-butoxyethanol. The binodal encountered at higher temperature is shown in Fig. 2.1. The system is miscible for temperatures below the binodal, and it demixes into two phases when heated. We can prepare samples at room temperature which is a major advantage of this system.

Experiments can be run in a temperature range between 25 °C and 50 °C which is convinient as the water that is used to control temperature will not evaporate too much. The coexistence curve (binodal) in the phase diagram was measured[1] by Martin Rohloff [15]. A fourth order polynomial was fitted to the right branch of the binodal and a sixth order polynomial to the left branch (see Fig. 2.1). Results from the fit were used to determine compositions for a given temperature. Material parameters depend on composition and temperature and are given in the appendix. This includes density, viscosity, diffusion coefficient, interfacial tension and molar volume.

2.2 Thermodynamic Driving

2.2.1 Constant Driving Revisited

As shown in Sec. 1.2 phase separation can be driven by a change in temperature. When it comes to quantitative analysis of the demixing process the choice of temperature ramps is an important matter. In this section I will present temperature ramps that are developed for a constant driving. The derivation is based on theoretical considerations of Auernhammer et al. [2].

For a deeper understanding of what drives the phase separation it is worth to consider the time evolution of composition $\phi(\vec{x}, t)$. It can be described by a diffusion equation [2, 4]:

$$\frac{d\phi}{dt} = \nabla[D(\phi, T)\nabla\phi].\tag{2.1}$$

Here D is a diffusion coefficient. In general it depends on composition ϕ and temperature T. The supersaturation σ of the system can be characterized by the difference of the actual composition from equilibrium composition:

$$\sigma = \frac{\phi - \bar{\phi}}{\phi_0},\tag{2.2}$$

where $\bar{\phi}(T)$ is the average composition of the coexisting phases, and $2\phi_0(T)$ is the width of the miscibility gap. In terms of the difference of the compositions $\phi_r(T)$ and $\phi_l(T)$ of the coexisting phases for the right and the left branch of the binodal

---

[1] See Sec. 3.2 for a description the phase transition measurements.

they are given by:

$$\phi_0(T) = \frac{\phi_r(T) - \phi_l(T)}{2} \,, \tag{2.3}$$

$$\bar{\phi}(T) = \frac{\phi_r(T) + \phi_l(T)}{2} \,. \tag{2.4}$$

The supersaturation σ takes the values ± 1 if the system is at equilibrium, and smaller absolute values if it is supersaturated. It turns out that $D(\phi, T) \sim \tilde{D}(\sigma)$. Therefore solving (2.2) for ϕ and inserting it in (2.1) gives

$$\frac{d\sigma}{dt} = \nabla[\tilde{D}(\sigma)\nabla\sigma] - (\zeta + \sigma\xi)\,. \tag{2.5}$$

The first term on the right side is again a diffusion term while the second term denotes a source strength for supersaturation. In the source term two parameters are introduced:

$$\zeta = \frac{1}{\phi_0} \cdot \frac{\partial\bar{\phi}}{\partial t}\,, \tag{2.6}$$

$$\xi = \frac{1}{\phi_0} \cdot \frac{\partial\phi_0}{\partial t}\,. \tag{2.7}$$

The latter, ξ, contains the contribution that follows from a changing width of the miscibility gap $2\phi_0$, and ζ accounts for the change in average composition $\bar{\phi}$.

Oscillations in the demixing of a binary fluid were first found in experiments on microemulsions that were performed with linear temperature ramps [19]. In contrast to microemulsions such a driving produces only a few oscillations in binary mixtures. In [2] this rapid decay for constant heating rates was connected to a decreasing of the source strength $\xi + \sigma\zeta$ in Eq. (2.5) in time due to a steeper slope of the coexistence curve. A constant thermodynamic driving throughout the entire heating process is achieved by a constant production of supersaturation that is characterized by ξ and ζ.

Based on these ideas the driving of the system was further developed. In their experiments Tobias Lapp and Martin Rohloff [8, 9, 15] used driving parameters that provide a constant driving for the individual top or bottom layer of the demixing fluid. The following derivation is adapted from [15].

Consider one layer (either top or bottom) with volume V and composition ϕ_b of the bulk phase. The composition of droplets in the bulk is given by ϕ_d. At time

t the system has a temperature T_1 and the compositions $\phi_b(T_1)$ and $\phi_d(T_1)$ of the two phases are the equilibrium compositions at the coexistence curve. At $t + \delta t$ temperature is shifted to $T_2 = T_1 + \delta T$ and the new equilibrium compositions would be $\phi_b(T_2) = \phi_b(T_1) + \delta\phi_b$ and $\phi_d(T_2) = \phi_d(T_1) + \delta\phi_d$. For a small time step δt the diffusion of the components between the two layers can be neglected. If one assumes that supersaturation is instantly removed by diffusion to droplets which grow by δV_d the conservation of volume requires:

$$V \cdot (\phi_b(T_2) - \delta\phi_b) = \delta V_d \cdot \phi_d(T_2) + (V - \delta V_d) \cdot \phi_b(T_2) \,. \qquad (2.8)$$

This can be rearranged to

$$\delta v_d = \frac{\delta V_d}{V} = \frac{\delta\phi_b}{\phi_d - \phi_b} \,. \qquad (2.9)$$

Next, both sides are divided by δt. For infinitesimal small time steps δt this gives

$$\dot{v}_d = \frac{1}{2\phi_0} \cdot \frac{d\phi_b}{dt} \,, \qquad (2.10)$$

which is the change in droplet volume fraction for one specific layer. Here equation (2.3) has been used to replace the composition of bulk and droplets by the width of miscibility gap.

For the iso-butoxyethanol-water system $\dot{v}_d$ denotes the supersaturation in the water-rich bottom layer if the composition of the left branch ϕ_l is used for ϕ_b. In this thesis I write ξ_l for $\dot{v}_d$ in the bottom layer to be consistent with notation previously used in publications [8, 9, 15]. A similar parameter ξ_r can be found for droplet growth in the top layer using the right branch of the phase diagram.

$$\xi_l = \frac{1}{2\phi_0} \cdot \frac{d\phi_l}{dt} \,, \qquad (2.11)$$

$$\xi_r = -\frac{1}{2\phi_0} \cdot \frac{d\phi_r}{dt} \,. \qquad (2.12)$$

These parameters are connected to (2.7) and (2.6) as $\xi = \xi_r + \xi_l$ and $\zeta = \xi_l - \xi_r$. In experiments one can keep either ξ_l or ξ_r constant, but not both at the same time. We decided to drive phase separation by controlling the parameter ξ_l and focus on precipitation oscillations in the bottom phase.

Temperature ramps can be calculated numerically for a fixed ξ. Equation (2.11) is

solved for the heating rate dT/dt:

$$\xi_l(t) = \frac{1}{2\phi_0} \cdot \frac{\partial \phi_l}{\partial T} \cdot \frac{\partial T}{\partial t} \,, \tag{2.13}$$

$$\Leftrightarrow \frac{dT}{dt} = \frac{2\xi_l(t)\phi_0(T)}{\frac{\partial \phi_l}{\partial T}} \,. \tag{2.14}$$

Integration of equation (2.14) is performed with the Euler method using time steps δt. This gives

$$T(t + \delta t) = T(t) + \frac{2 \cdot \xi_l(t) \cdot \phi_0(T)}{\frac{\partial \phi_l}{\partial T}|_{T(t)}} \cdot \delta t \,. \tag{2.15}$$

Values for $\phi_0(T)$ and $d\phi_l/dT|_T$ can be obtained from the measured binodal in the phase diagram in Fig. 2.1. The starting temperature T_0 is set to $25.8\,°\text{C}$. Temperature ramps are calculated until the temperature $T = 50\,°\text{C}$ is reached. A representative example is shown in Fig. 2.2

In the experiments where we study the influence of stirring we used temperature ramps with the constant value of $\xi_l = 2.5 \cdot 10^{-5}\,\text{s}^{-1}$ (see Fig. 2.2). For the sake of less cluttered equations I will always write ξ for ξ_l in the following.
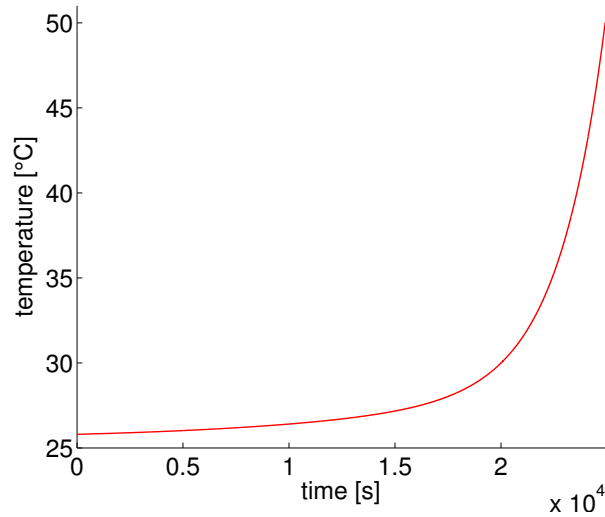

Figure 2.2: Temperature ramp for a value of $\xi_l = 2.5 \cdot 10^{-5}\,\text{s}^{-1}$ that was used in the stirring experiments. It was calculated with equation (2.15).

2.2.2 Prediction of the Oscillation Period

For a constant driving the period of oscillations can be predicted as follows [8]. Growth of droplets is supposed to be governed by two mechanisms: diffusion and coalescence. During diffusive growth ξ denotes the change in droplet volume fraction. It can be expressed in terms of droplet radius r and number density n_0:

$$\xi = \frac{d}{dt}\left(\frac{4}{3}\pi\, n_0 r^3\right) = 4\pi n_0 r^2 \dot{r}\,, \tag{2.16}$$

$$\Leftrightarrow \dot{r} = \frac{\xi}{4\pi n_0 r^2}\,. \tag{2.17}$$

For the growth by coalescence we consider the vertical velocity u of the droplet due to buoyancy forces:

$$u = \kappa r^2 \qquad \text{with} \qquad \kappa = \frac{2}{9}\frac{\Delta\rho \cdot g}{\eta}\,. \tag{2.18}$$

Here, $\Delta\rho$ is the density difference of the two phases, g is the gravitation acceleration and η is the viscosity of the bulk phase. A sedimenting droplet with radius r passes the volume $\pi r^2 \cdot ut$ within the time t. The volume fraction of small droplets within this volume is given by ξt. We introduce a collision efficiency ϵ because not all droplets in the path will merge with the large droplet. Thus the change in volume $\dot{v}$ of the falling droplet is determined by

$$\dot{v} = \epsilon \cdot \xi t \cdot \pi r^2 u\,. \tag{2.19}$$

Using $\dot{v} = 4\pi r^2 \dot{r}$, we get

$$\dot{r} = \frac{1}{4}\epsilon\kappa\xi t r^2\,. \tag{2.20}$$

We now combine (2.17) and (2.20) which yields:

$$\dot{r} = \frac{\xi}{4\pi n_0}\frac{1}{r^2} + \frac{\epsilon\kappa\xi t}{4}r^2\,. \tag{2.21}$$

Droplets first grow by r^{-2} until a minimum in $\dot{r}$ is reached, also referred to as the bottleneck in droplet growth. When the bottleneck is passed r diverges in finite time. The time until the droplets grow to infinity was taken for the oscillation period Δt.

Under reference to [8, pp 117-119] we may write:

$$\Delta t = \alpha \left(D\sigma\kappa^3 \right)^{-1/7} \xi^{-3/7} . \tag{2.22}$$

Here, D is the diffusion coefficient and σ is a length scale depending on interfacial tension γ, molar volume V_m, equilibrium concentration of the minority component ϕ_e, the universal gas constant R and the absolute temperature T:

$$\sigma = \frac{2\gamma V_m}{RT}\phi_e . \tag{2.23}$$

A proportionality between droplet density n_0 and ξ was assumed for the derivation:

$$\frac{\xi}{n_0} = \beta \cdot D\sigma , \tag{2.24}$$

with β being a proportionality factor. All material constants are functions of the temperature T and therefore $\Delta t = \Delta t(T)$. One finds that Δt decreases in time (see e.g. Fig. 4.2). The prefactor α is gained from a fit to the data of measurements with constant ξ:

$$\alpha = 0.68 \pm 0.20 . \tag{2.25}$$

2.2.3 Time-Dependent Driving

In my second series of measurements I looked at the response of the system to a time-dependent driving. Equation (2.15) can also be applied in the general case where ξ is a function of time.

I used temperature ramps where $\xi(t)$ is a square-wave with alternating values ξ_{min} and ξ_{max}. It has the advantage that the theory which was derived for constant ξ can still be applied piecewise. These ramps are classified by an average value $\bar{\xi}$, a relative amplitude $A = (\xi_{max} - \bar{\xi})/\bar{\xi}$, and a period Δt_ξ for the oscillation in ξ. However, even for a constant ξ the period Δt of oscillations in precipitation decreases in time due to the temperature dependence of the material parameters (cf. Eq. (2.22) with time-dependent material parameters provided in the appendix). This means that if Δt_ξ is the same for the entire temperature ramp the ratio of the two periods changes. Similar to the constant ramp rate ξ, I wanted to fix the driving conditions for the oscillatory ξ throughout the measurement. Thus I decided to keep the ratio $p := \Delta t/\Delta t_\xi$ a fixed value. This means that Δt_ξ has to decrease with proceeding time.

Based on the prediction (2.22) for the period of precipitation $\Delta t(T)$ we hence modify the calculation of temperature ramps. As an input for the nummerical integration $\bar{\xi}$, A, and p are needed. Because ξ is chosen to be a square wave the calculation of $T(t)$ can be performed as before using either ξ_{max} or ξ_{min} in equation (2.15). The period $\Delta t_\xi(t)$ is calculated at the start of one ξ period:

$$\Delta t_\xi(t) = \frac{\Delta t[T(t), \xi(t)]}{p} \ . \tag{2.26}$$

After the time interval $\Delta t_\xi/2$ the value of ξ is changed and the period is recalculated for the new value. This is repeated until the final temperature of $50\,°C$ is reached. A typical ramp with time-dependent driving is shown in Fig. 2.3 for $\bar{\xi} = 2.5 \cdot 10^{-5}\,\text{s}^{-1}$, $A = 0.2$ and $p = 0.5$. The physical meaning of $p = 0.5$ is that a full period of precipitation is expected in half a period of $\xi(t)$ which is an interval of constant ξ. It should be noted that as a consequence the time intervals for ξ_{max} are in average shorter than for ξ_{min}, because the driving is more effective for higher ξ.
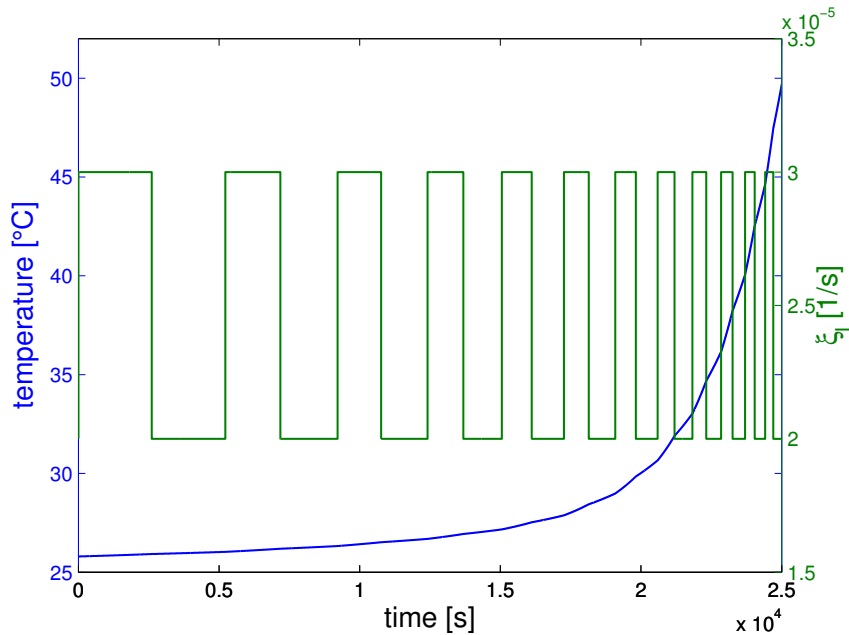

Figure 2.3: Temperature ramp for time-dependent driving. $T(t)$ (blue) and $\xi(t)$ (green). Parameters are $\bar{\xi} = 2.5 \cdot 10^{-5}\,\text{s}^{-1}$, $A = 0.2$, and $p = 0.5$.

3 Experimental Techniques

I studied the demixing of water and iso-butoxyethanol by measuring the turbidity of the system, that is the intensity of light scattered at droplets. Turbidity measurements can be performed with a simple optical setup and require little effort in image processing. Unfortunately, though, a connection between the intensity of scattered light and the droplet size and number is not trivial for polydisperse droplets [18].

3.1 Setup

A mixture of water and iso-butoxyethanol with a composition close to the critical composition is filled into measurement cells (10 mm $\times$ 10 mm $\times$ 35 mm) made by Hellma GmbH. The cells are sealed with teflon tape and mounted into a water bath. Water temperature is controlled by a combination of a Haake EK20 immersion cooler and a Huber CC-E immersion thermostat. Additionally the temperature is measured with a PT100 temperature sensor. The sample is illuminated by a cold light source (KL 2500 LCD, Schott) at an angle of 20° to the view axis as illustrated in Fig. 3.1(b). A CCD camera (BM-500CL) with a zoom lense is used for image acquisition. The water bath is partially covered with black sheet on the outside in order to reduce stray light.

A stirring bar inside the cell can be controlled by a magnetic stirrer (IKAMAG RET control-visc C) under the water bath (see Fig. 3.1(a)) which can be operated at stirring rates in a range between 50 rpm and 1500 rpm. Stirring bars of two different sizes were used in the experiments: A small stirring bar (diameter: 2 mm, lenght: 2 mm) was used to study the influence of moderate stirring to the demixing process. It was however too small to mix the two phases completely. Thus the sample had to be shaken by hand before each measurement in order to homogenize it. For temperature ramps where no stirring was applied we replaced the stirring bar with a bigger one (diameter: 3 mm, length: 6 mm). Mixing at 1500 rpm for one hour is then sufficient to homogenize the sample.
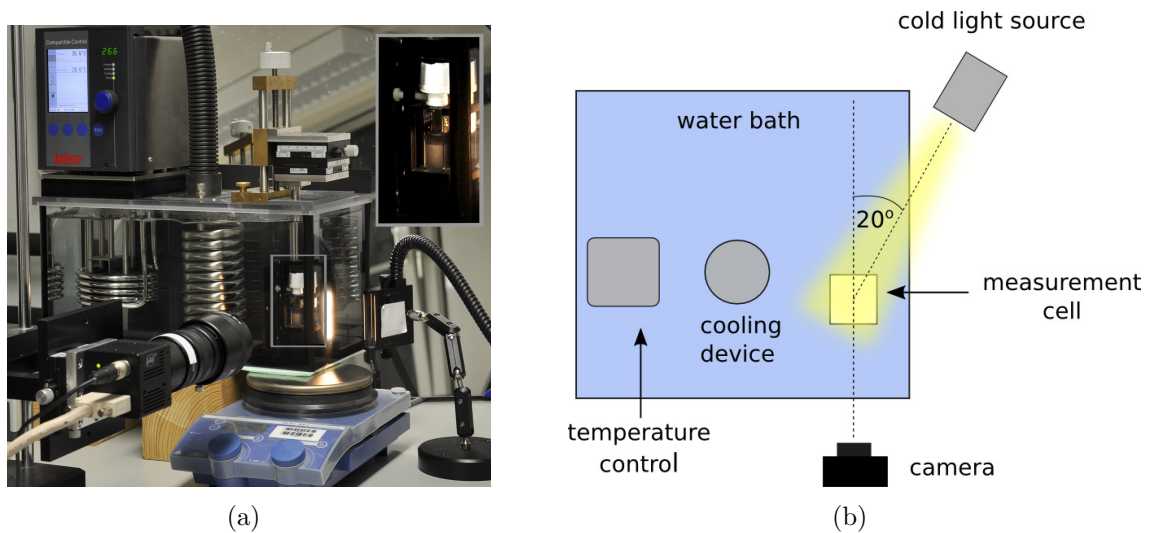
Figure 3.1: (a) Front view of the experimental setup with a close-up of the measurement cell and (b) schematic top view.

The temperature control, the camera, and the magnetic stirrer are connected to a computer. A LabVIEW program enables fully automated measurements.

3.2 Measurement of the Transition Temperature

The temperature at which the transition from one homogeneous phase into two separated phases takes place can be obtained from the phase diagram in Fig. 2.1 for a given composition ϕ. However, the position of the critical point might be slightly shifted due to impurities. Thus the transition temperature is measured everytime a new sample is prepared. The measurement is repeated for samples that have been in use for a longer time.

Measurements of the transition temperature are performed with linear temperature ramps that start below the expected transition temperature. The camera objective is used to zoom in on the measurement cell. From the taken images the mean grey value is calculated (blue curve in Fig. 3.2). Two lines are fitted to the turbidity curve: one in the region of moderate increase in the beginning and one in the region of strong increase (red lines in Fig. 3.2). Each line is defined by manually selecting two points on the turbidity curve. The transition temperature is the temperature that corresponds to the intersection point of the lines (vertical black line in Fig. 3.2).
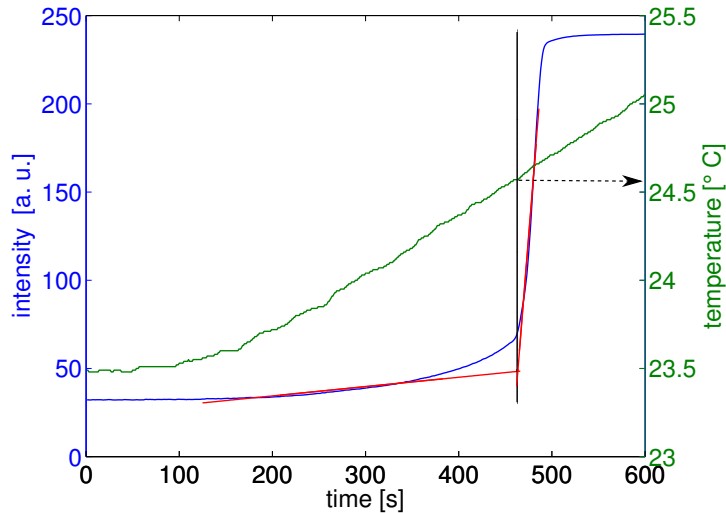
Figure 3.2: Turbidity of the sample (blue) and temperature measured by the thermostat (green) are plotted against time. Straight lines (red) fitted to the turbidity curve determine the transition temperature.

3.3 Measurement of Turbidity Oscillations

For oscillation measurements the zoom lense is tuned such that the whole measurement cell is pictured. The sample is homogenized below the transition temperature either by the use of a magnetic stirrer or by hand. Subsequently, the sample is heated 0.2°C above the transition temperature which leads to a first separation into two phases. For 180 minutes the sample is relaxed so that it approaches equilibrium again with a defined interface between the water-rich bottom layer and the iso-butoxyethanol-rich top layer. Then a temperature ramp as described in Sec. 2.2 is run. While the heating is applied pictures are taken at a constant frame rate. After reaching the final temperature of 50°C the sample is cooled down to 25°C again.

3.4 Data Analysis

A set of pictures (Fig. 3.3) obtained from turbidity measurements shows a typicial precipitation event in the water-rich phase of the sample. Dark regions in the pictures indicate that the fluid is transparent and brighter regions indicate turbidity resulting from droplets. At the start the liquid mixture consists of two spatially separated phases (Fig. 3.3(a)). The bottom phase can be indicated as the water-rich phase of higher density while the less dense iso-butoxyethanol-rich phase is on top. Due to a

temperature-induced supersaturation droplets of the iso-butoxyethanol-rich phase nucleate within the water-rich phase. This gives rise to an increasing turbidity in the bottom layer (Figs. 3.3(b)-3.3(d)). As the droplets grow bigger gravitation becomes more important and finally causes the droplets to sediment towards the interface (Figs. 3.3(e)-3.3(f)). At the end of one precipitation cycle the bottom layer is almost transparent again (Fig. 3.3(g)). A similar process can be observed in the upper layer of the sample. However, in general the oscillation period is different for the top and bottom layer.
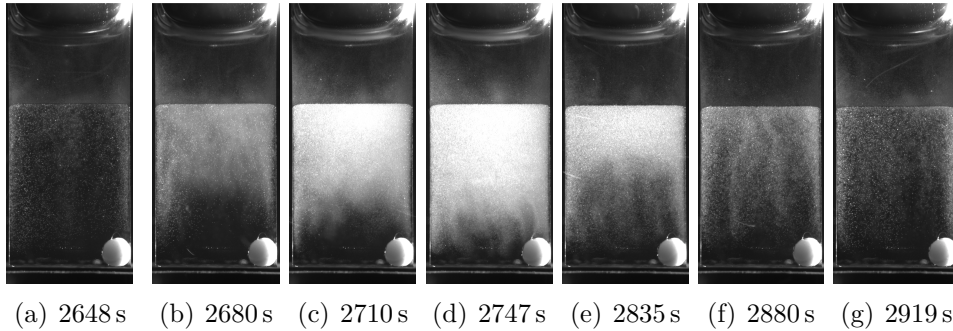

(a) 2648 s   (b) 2680 s   (c) 2710 s   (d) 2747 s   (e) 2835 s   (f) 2880 s   (g) 2919 s

Figure 3.3: One oscillation in detail: (a) Start of oscillation. The bottom phase is not turbid. (b-d) turbidity increases due to droplet growth. (e-f) Sedimentation sets in and the turbidity decreases. (g) The system is again not turbid as it was in (a). Note that the interface has slightly shifted. The images cover a time interval of about 30 minutes and temperatures between 26.6°C and 27.8°C. The measurement was performed with a mixture of iso-butoxyethanol and water (composition $\phi = 0.28$) for a driving rate of $\xi = 2.5 \cdot 10^{-5}\,\mathrm{s}^{-1}$. A stirring bar is located in the bottom right corner but not activated.

During one temperature ramp there are usually 4000 images taken. The important information that has to be drawn out of these data is the evolution of turbidity. For this aim space-time plots as described by Auernhammer et al. [2] are constructed. They are obtained in the following way: gray values of every image are averaged horizontally. Thus one image is reduced to a vertical line of pixels. All these lines are put together into a new image with time proceeding from the left to the right. One point in the space-time plot indicates the average turbidity at a given height of the sample and at a given instant of time. An examplary space-time plot is shown in Fig. 3.4.

Next the changing height of the interface is identified in the space-time plots. This is done by manually selecting points on the curve that represent the interface and connecting them smoothly. For each time step grey values of 10 pixels at a distance
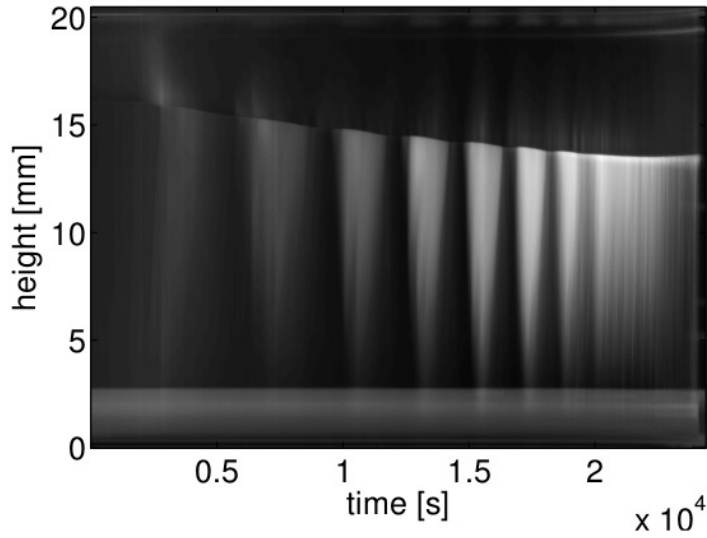
Figure 3.4: Exemplary space-time plot for a measurement of turbidity (gray scale) as a function of height and time. The sample is not stirred and heated with constant $\xi = 2.5 \cdot 10^{-5}\,\mathrm{s}^{-1}$. The bright band at the bottom is caused by the presence of the stirring bar. Images in Fig. 3.3 can be assigned based on times in their respective captions (sixth period of oscillation in bottom phase).
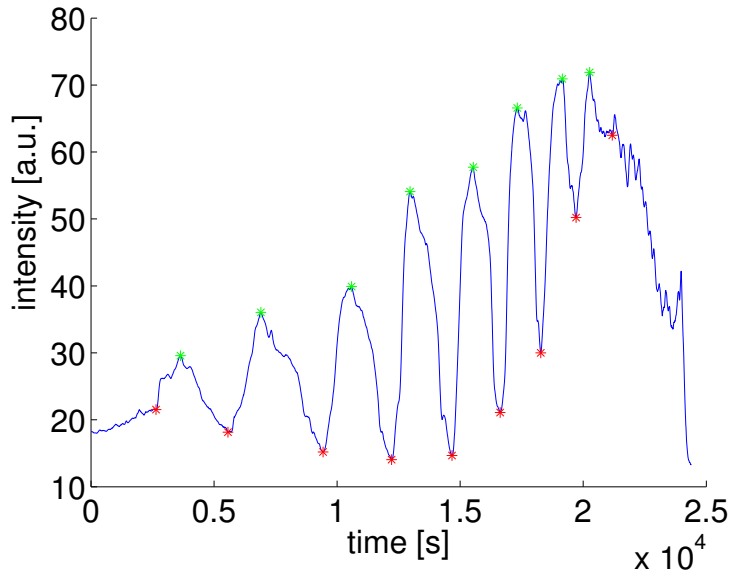
Figure 3.5: Time evolution of turbidity in the bottom phase obtained from space-time plot in Fig. 3.4. Grey values 50 pixels ($\approx 0.5\,\mathrm{mm}$) below the meniscus are plotted against time. Minima (red) and maxima (green) are identified.

of 50 pixels above and below the determined meniscus are averaged. By plotting these values against time, one gets a quantitative time evolution of turbidity for the top phase and the bottom phase, respectively (see Fig. 3.5 for exemplary turbidity curve in the bottom phase). In the turbidity graph minima are manually detected and the maxima are determined as the absolute maxima between two minima.

4 The Influence of Stirring

Experiments [21] and simulations [3] suggest that the background flow does not influence the period of oscillations in binary phase separation. We systematically tested this prediction in a series of measurements We vary the flow in the sample by stirring at different rates. The period of oscillation is measured and compared to the prediction given by Eq. (2.22).

For experimental realization we add a small magnetic stirrer (diameter: 2 mm, length: 2 mm) to the measurement cell. Stirring is applied throughout the temperature ramp at a constant stirring rate. We use a temperature protocol that is designed for a constant driving in the bottom layer of the system (see Sec. 2.2) because the stirring bar is located at the bottom of the cell. For all measurements the same driving parameter $\xi = 2.5 \cdot 10^{-5}\,\mathrm{s}^{-1}$ is chosen.

We take measurements with stirring rates of 60, 90, 120 and 180 revolutions per minute. As a reference some measurement are also carried out without stirring. One temperature ramp takes about 7 hours and additionally the sample is relaxed 3 hours before a ramp starts. We can not run more than one ramp consecutively because the sample has to be remixed by hand after each measurement. As each measurement was repeated at least once, it took several weeks to collect the data. In between we replaced the sample with a new one. Fig. 4.1 shows representative turbidity curves for measurements with 120 rpm and without stirring.

Data analysis as described in Sec. 3.4 is applied to determine the maxima and minima in turbidity. The period of oscillation Δt is calculated as the time between two consecutive minima in turbidity. Here it is implied that a precipitation event is finished when the fluid layer is cleared again. It is also possible to use the maxima in turbidity for the calculation of Δt.

In Fig. 4.2 the measured periods for different stirring rates are shown. All measurements that are run with stirring rates between 60 rpm and 180 rpm are included which means that data points for one stirring rate represent up to three temperature ramps. A prediction for the oscillation period is obtained from (2.22) and also plotted
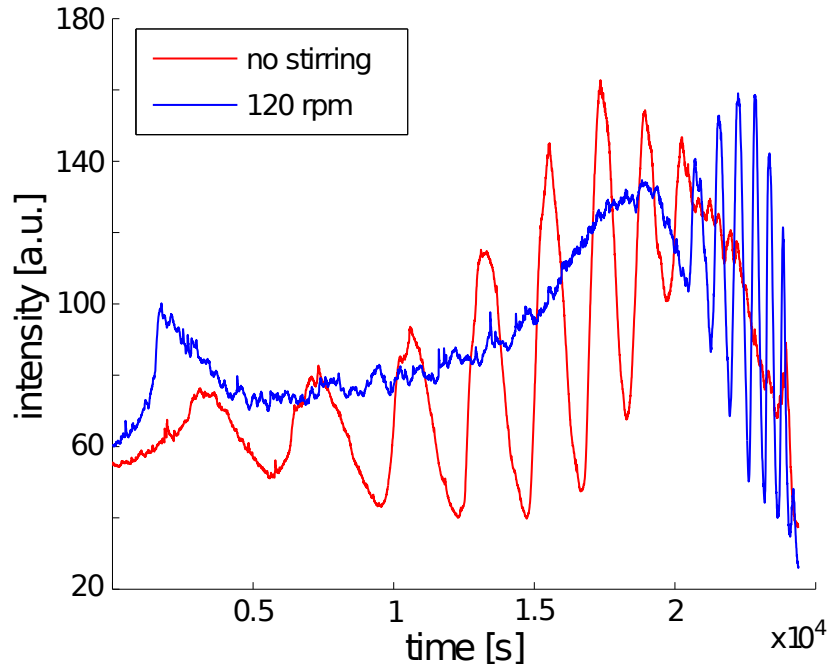
Figure 4.1: Turbidity in the bottom layer for a measurement with 120 rpm and for a measurement without stirring. For the stirring rate 120 rpm the first oscillations are observed at time $2 \cdot 10^4$ s.

in Fig. 4.2. One can see that the data points roughly follow the prediction. (A larger derivation for early times is also observed in experiments without stirring). The experimental data suggest that the dependency of Δt is not influenced by moderate stirring.

On the other hand there is a nontrivial trend in the data: oscillations start at later times when the sample is stirred. Instead of oscillations a general increase in turbidity is observed at early times (see $t < 2 \cdot 10^4$ s for a stirring rate of 120 rpm in Fig. 4.1). Presently, however, it is difficult to make a quantitative statement about this trend. The times for which the first minimum appear in the turbidity are compared for different measurements (blue stars in Fig. 4.3). Our results do not confirm a clear relation between start of oscillations and stirring rates. Moreover, if the third minima are taken into account (green squares in Fig. 4.3) one finds that there is a substantial variability of the instance when the first oscillation is observed in different experiments at a given stirring rate of 60 rpm, 90 rpm and 120 rpm. For the same stirring rate the starting time of oscillations can vary in a range of three oscillations. This is in some cases a larger variation as for measurements with different stirring rates (for example 120 rpm and 180 rpm). To some extent this
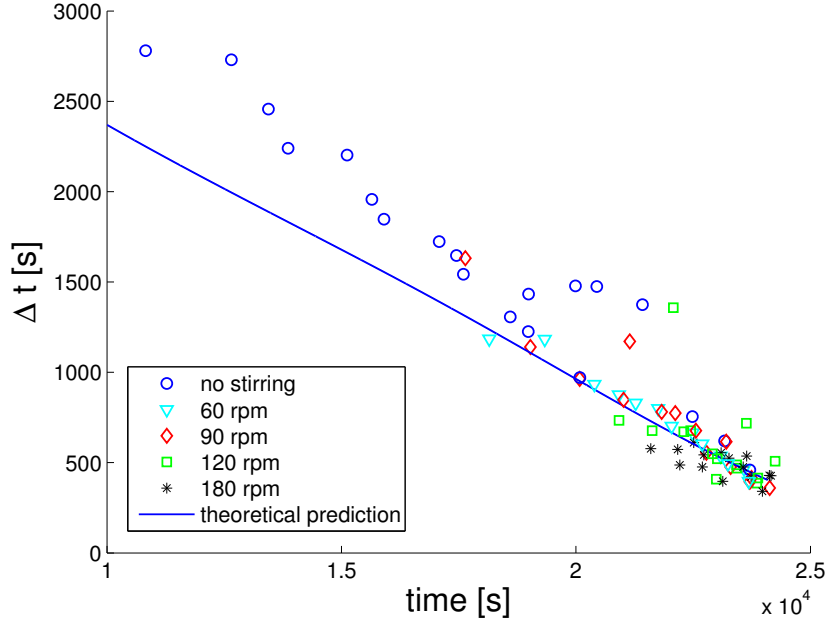
Figure 4.2: Oscillation period Δt in the bottom layer is plotted against time for a constant driving parameter $\xi_l = 2.5 \cdot 10^{-5}\,\mathrm{s}^{-1}$. Different stirring rates are specified in the legend, and additionally the theoretical prediction for Δt is given by a solid line.

may be due to the fact that it is not always possible to clearly identify minima and maxima of turbidity. However, we expect that the trend might be more clearly accessible in experimentally realizing even smaller stirring rates, and combining turbidity measurements with particle tracking. More experiments will be needed to clearly address this dependence.

Finally we note that the oscillations disappear for higher stirring rates. Thus we run experiments with 600 rpm. Indeed no oscillations are visible under this condition. In Fig. 4.4 a space-time plot and the corresponding turbidity curve for a stirring rate of 600 rpm are shown.
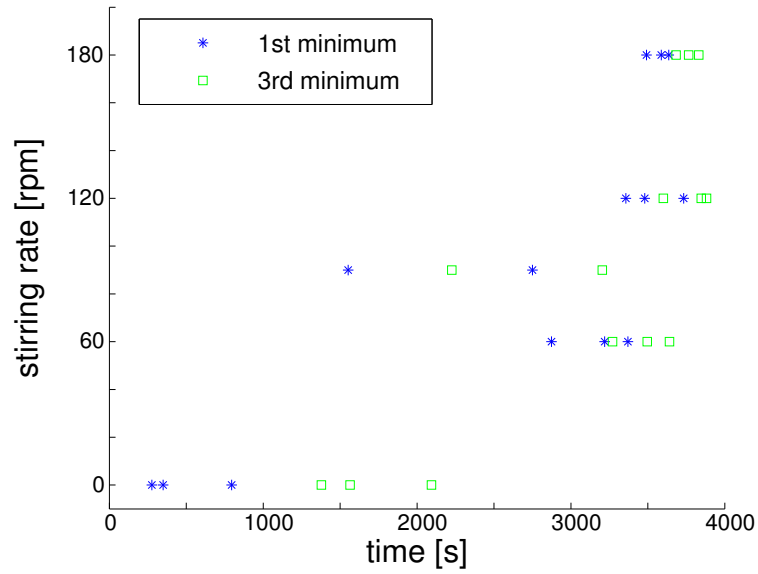
Figure 4.3: Start of oscillations for different stirring rates. The times for which a first minimum in turbidity was observed are plotted. For a better comparison the third minimum is also shown. Each data point represents one temperature ramp.

Figure 4.4: (a) Space-time plot and (b) turbidity for a measurement with 600 rpm stirring. No oscillations can be observed in the stirred bottom layer which is permanently turbid (red curve in (b)). The top layer is less turbid (in the space-time plot it appears nearly black). Still one can observe small oscillations (blue curve in (b)) because the stirring only affects the bottom layer.

5 Time-Dependent Driving

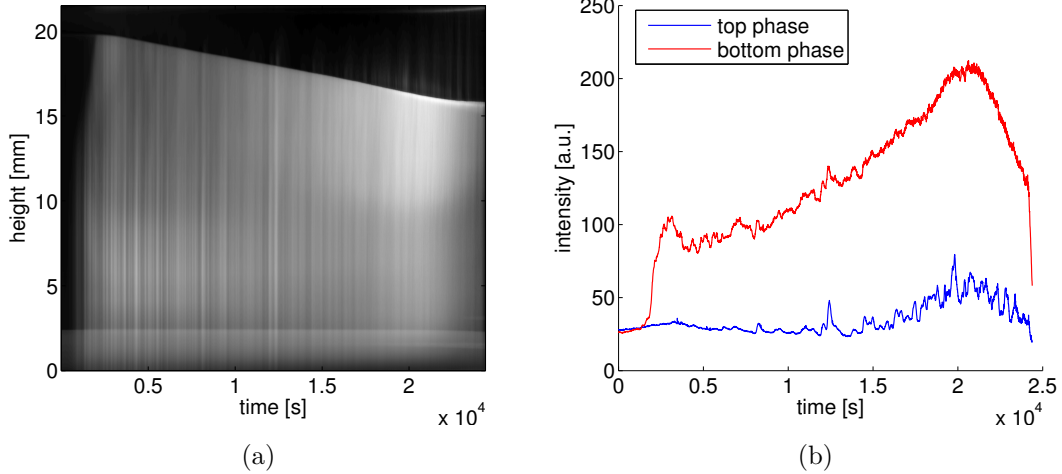In this section I will present results from measurements with a time-dependent driving parameter ξ. I used a square wave function with an average value $\bar{\xi}$ and a relative amplitude A, as described in Sec. 2.2.3. To allow for a better comparison I used the same value for average driving $\bar{\xi} = 2.5 \cdot 10^{-5}\,\mathrm{s}^{-1}$ in all experiments and varied the parameters A and p.

5.1 Consistency Check

At the beginning I tested the time-dependent driving for $p = 0.5$ and a small amplitude. By the way that we constructed the temperature ramps, we expected to observe one precipitation event in each period of constant ξ for this set of parameters. For analysis of the measurement both the turbidity and ξ are plotted against time in Fig. 5.1. It can be seen that for the first part of the temperature ramp the turbidity period is exactly as we expected. At the end though there is one turbidity oscillation in a full oscillation of ξ. On the one hand this gives evidence that the calculation of temperature ramps was carried out correctly. On the other hand it points to the possibility of interesting phase locking effects as a function of p, A and t.

5.2 Observation of 1:1 Phase Locking

The oscillating ξ can be understood as a periodic external force on the precipitation oscillations. The undisturbed 'oscillator' would be the system with a constant driving. However, this term should be handled with care as its period and amplitude are not constant but changing in time. As mentioned in Sec. 2.2.3 the time dependence of the period Δt (see e. g. Fig. 4.2) is taken into account in the calculation of temperature protocols. Synchronization theory then predicts a phase locking scenario if the external force has a frequency close to the frequency of the undisturbed oscillator. The periods of precipitation and the external force should be the same for $p = 1$.
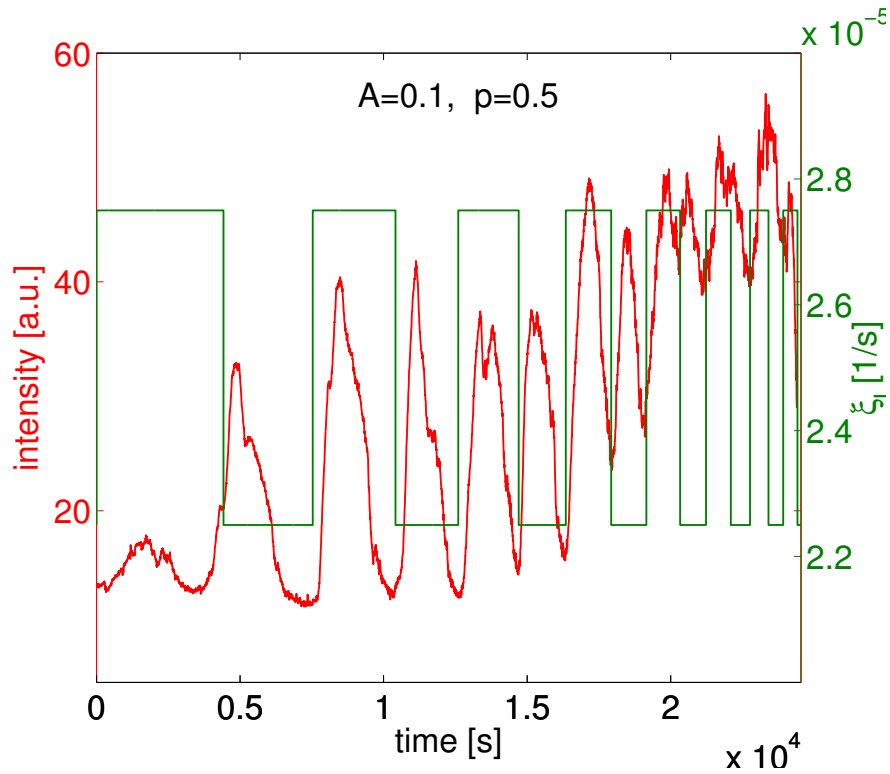
Figure 5.1: Turbidity and ξ for a measurement with $A = 0.1$ and $p = 0.5$. In most cases one precipitation event occurs within each interval of constant ξ which provides a consistency check for the construction of the temperature ramps.

Thus we ran experiments with $p = 1$ and varied the amplitude A to check for this prediction of a 1:1 phase locking.

5.2.1 Fixed Amplitude $A = 0.2$

First we will discuss results from experiments with an amplitude $A = 0.2$. Here we observe oscillations in turbidity that perfectly match with the oscillations in ξ. In Fig. 5.2 we demonstrate that the period of oscillation follows the prediction for $\bar{\xi}$ quite well. This is expected since it was used to calculate the period of ξ oscillations. The plot indicates period of turbidity oscillation Δt as a function of the time t where the minimum of oscillation is observed. One can see that the data points are clustered for $t > 2 \cdot 10^4$ s which means that the positions of minima are similar for independent measurements. This points to a phase locking scenario.

A phase locking for $p = 1$ and $A = 0.2$ can clearly be seen in Figs. 5.3: We plotted the turbidity curve for subsequent time intervals of ξ periods. The time axis was

rescaled so that values between 0 and 0.5 represent driving with ξ_{max} and values between 0.5 and 1 represent driving with ξ_{min}. If one takes a closer look at the characteristics of turbidity oscillation in Fig. 5.3(c) it becomes obvious that the minima of turbidity appear in the regime of high ξ while maxima are observed in the other regime. We first noticed this for temperature ramps that start with a period of high ξ. It was then checked for temperature ramps that start with the opposite phase (see Fig. 5.3(d)). Here the first maxima were found in the ξ_{max} phase but for later times they shift to the ξ_{min} phase as well. This provides strong evidence for phase locking.

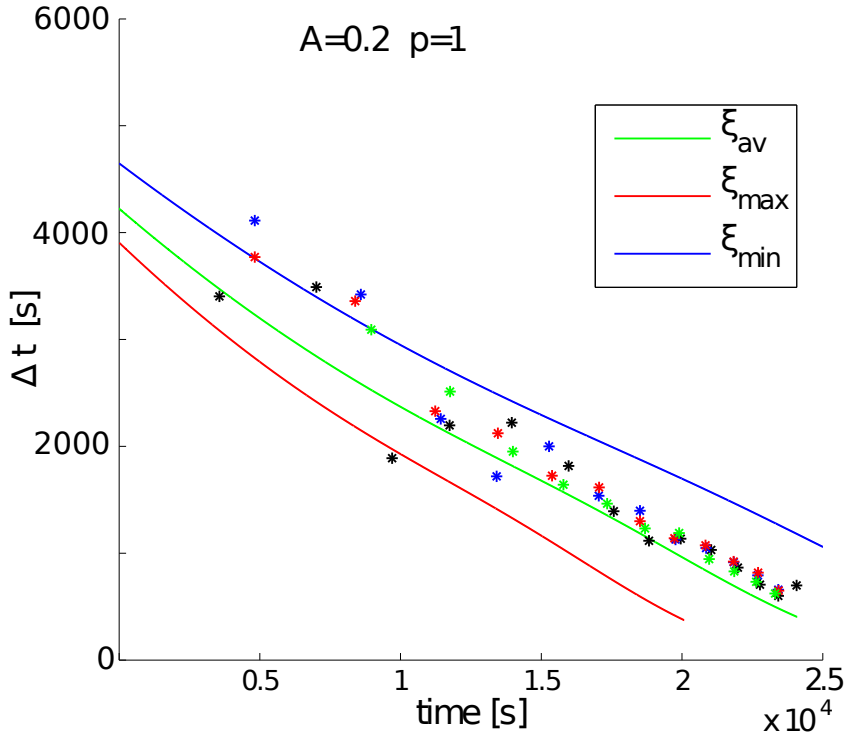**Figure 5.2:** Oscillation period Δt for measurements with $A = 0.2$ and $p = 1$. Data points with the same color belong to one temperature ramp. Especially for later times the measured data points follow the period of external driving which is the prediction for average ξ (green line) very well. For comparison the prediction for maximum and minimum values of the oscillating ξ are also shown.

5.2.2 Variation of Amplitude

Next we wanted to know, if the phase locking can also be observed for other amplitudes. We checked for two smaller amplitudes: For a measurement with $A = 0.1$ (see Fig. 5.4(b))eleven out of twelve observed maxima are located in the low ξ phase and for a measurement with $A = 0.05$ (see Fig. 5.4(a))it is only ten out of twelve maxima. A closer look reveals that this is due to a small mismatch of the period and to resulting *phase slips* in the precipitation oscillations. One could therefore argue that for smaller amplitudes we are not yet in the synchronization region but at the border. We also ran experiments with a high amplitude of $A = 0.5$ (see Fig. 5.4(d)). For this amplitude phase locking is clearly observed.

5.2.3 Slight Variation of p

It might be worth to test if there is still a 1:1 phase locking for a driving period that is different from 1. For a classical oscillator with periodic external forcing one would expect to see synchronization in the region of an Arnold tongue. We indeed observe phase locking for the parameters $A = 0.1$ and $p = 0.89$ (see Fig. 5.5). It takes some oscillations though to reach the synchronized state.

If we move further away from $p = 1$ the synchronization seems to vanish. For $p = 0.81$ and $A = 0.2$ (see Fig. 5.6) the frequencies seem to be in phase for the first five periods but a closer look reveals that the phase is shifted for later times. This indicates that the system is outside the synchronization region. However, we consider an oscillator with changing amplitude, and thus, the theory for a classical driven oscillator might not apply. There is more theoretical work needed to resolve this.
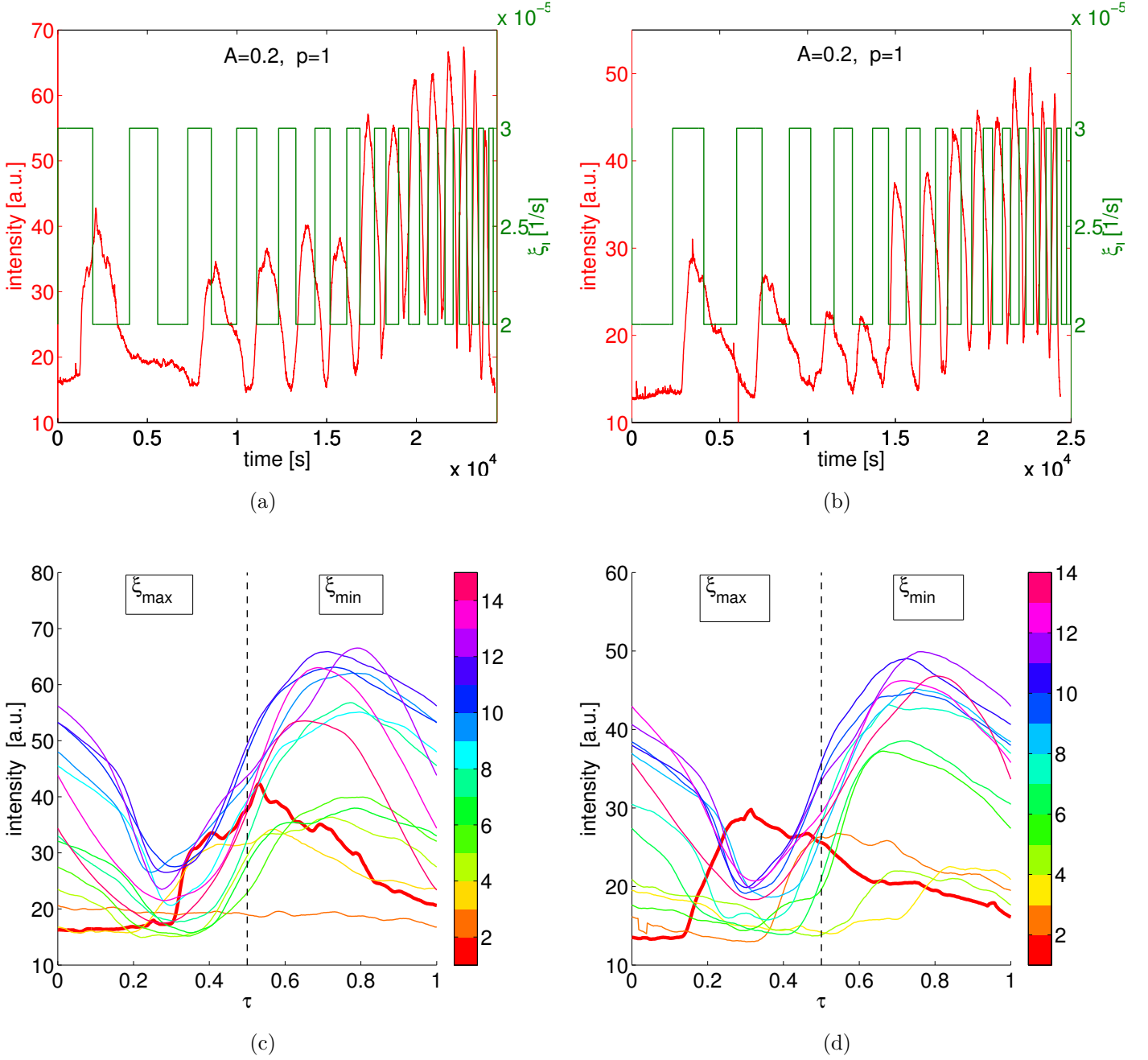
Figure 5.3: (a) and (b): Turbidity and ξ oscillations for two measurements with $A = 0.2$ and $p = 1$. The ramp in (a) starts with ξ_{max} and the ramp in (b) with ξ_{min}.

(c) and (d): Turbidity of one temperature ramp is rescaled for the time intervals of one period in ξ. Values of $0 < \tau < 0.5$ on the time axis represent periods of driving with ξ_{max} and values in the range $0.5 < \tau < 1$ represent periods of ξ_{min}. The colors encode subsequent time intervals. Plots in (c) and (d) are obtained from (a) and (b), respectively. For both scenarios one observes a clear 1:1 phase locking although the first peak (red curve) appears in different regimes.
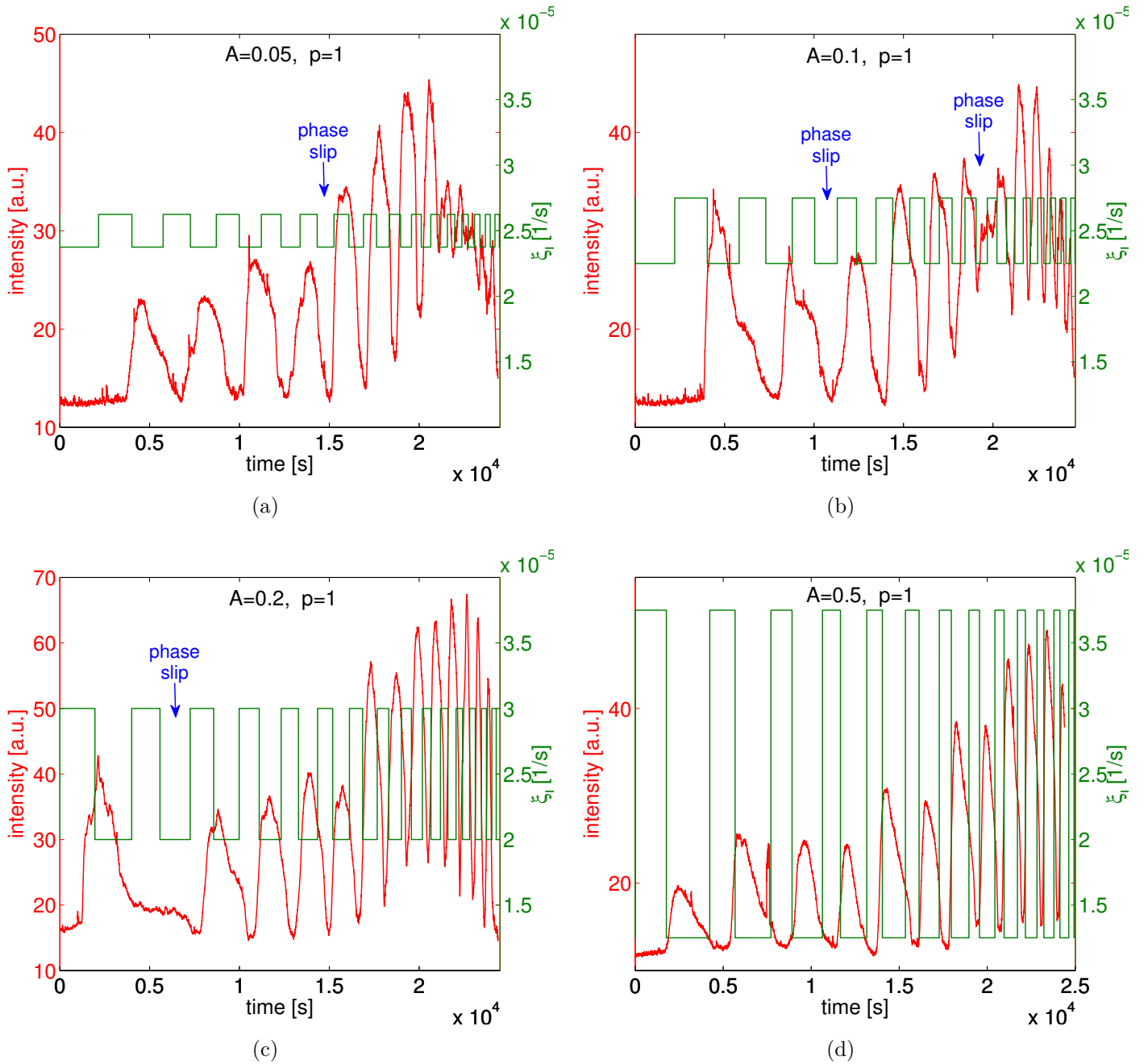
Figure 5.4: Turbidity curves for different ramp parameters. From (a) to (d) the amplitude increases, but $\bar{\xi} = 2.5 \cdot 10^{-5}\,\mathrm{s}^{-1}$ and $p = 1$ are kept constant. In (a) and (b) driving starts with ξ_{max} and contrary with ξ_{min} in (c) and (d). The expected 1:1 phase locking can be observed for a high amplitude. For smaller amplitudes there are phase slips in the turbidity oscillations. In (c) the second period is skipped completely while in (a) the phase slip appears over more than one period.
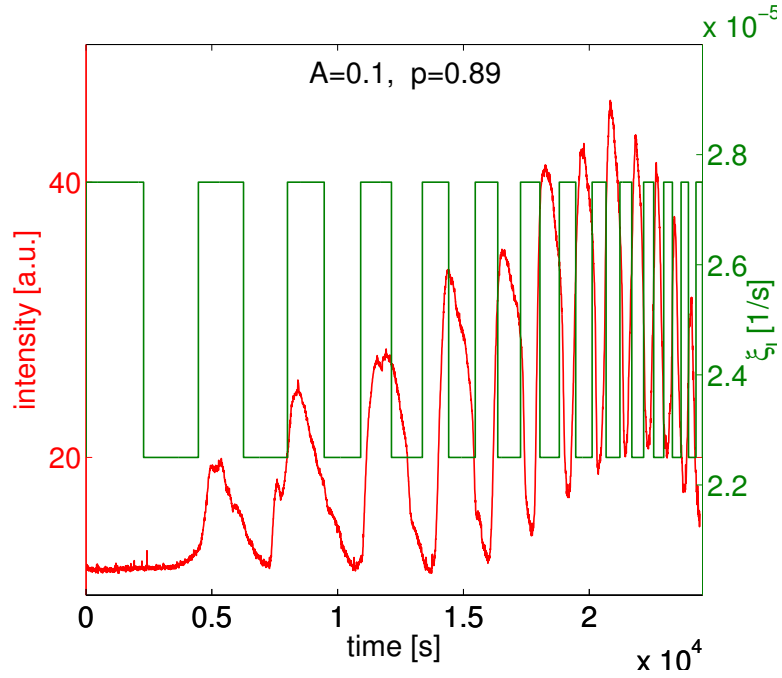
Figure 5.5: Turbidity and ξ for a small amplitude $A = 0.1$ and a driving period that is slightly different from 1. One still observes a 1:1 phase locking, but it takes four periods until the synchronization is observed.

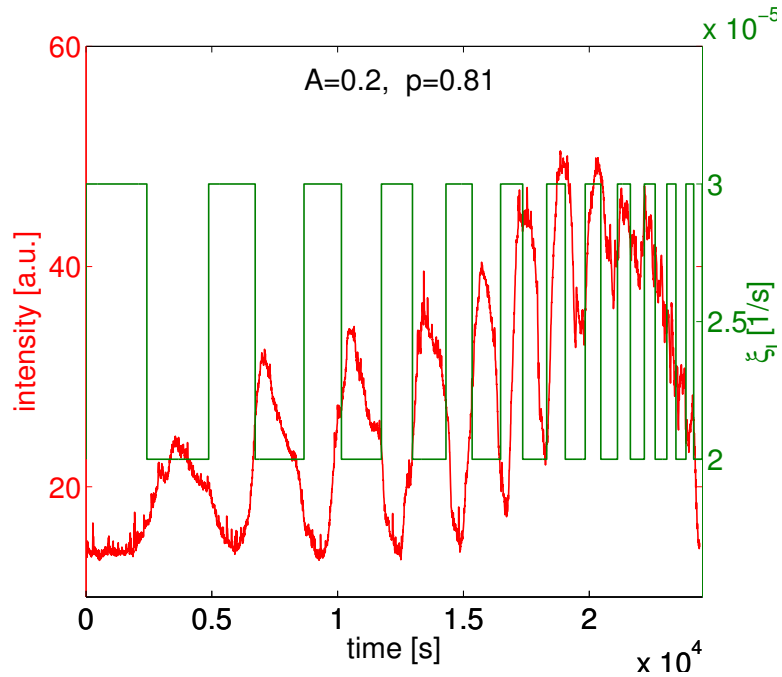**Figure 5.6:** Turbidity and ξ for an intermediate amplitude $A = 0.2$ and a driving period of $p = 0.81$. The turbidity oscillations do not synchronize, the oscillations are in phase only for the first periods.

5.2.4 Selection of the Phase: A Theoretical Approach

Still the question remains why exactly we see maxima in the region of low driving and minima in the region of strong driving. This can be answered by considering the model for droplet growth described in Sec. 2.2.2. Inserting (2.24) into (2.21) and multiplying with $4\pi r^2$ yields:

$$4\pi r^2 \dot{r} = \beta D\sigma + \pi\epsilon\kappa\xi tr^4, \tag{5.1}$$

with the change of droplet volume $\dot{v} = 4\pi r^2\dot{r}$ on the left-hand side. The growth for early times is governed by the term $\beta D\sigma$. It is reasonable to assume that all parameters are approximately constant over one period of precipitation. Thus in the beginning the volume change is constant and independent of ξ. For later times the term $\pi\epsilon\kappa\xi tr^4$ is dominant, and the growth is strongly affected by ξ. Using this we can qualitatively analyze the phase shift for a 1:1 driving assuming that synchronization is given.

Consider the droplets start to grow at the beginning of an interval with low driving. At first the growth of droplets is linear in time and not dependent on the driving force. The actual value of ξ becomes important in the subsequent stage of a high driving. The droplets grow faster than they would for the average ξ, which leads to shortened period of precipitation.

On the other hand, if droplet growth starts at the beginning of an interval with strong driving, the value of ξ will first matter for the subsequent stage of low driving. In this case the period of precipitation would be longer than that for the average ξ.

Both scenarios lead to a shift of the starting time into the region of strong driving. This is exactly what we observe in experiments if one assumes that the starting time of droplet growth corresponds to a minimum in turbidity.

5.3 Phase Locking For Different Driving Periods

Having found synchronization for the trivial case where $p \approx 1$ we expand the search for phase locking in the parameter space defined by amplitude A and period p. For higher amplitudes it is most likely to find synchronisation. However, it is not clear a priori how this looks in detail.

5.3.1 Driving Period $p = 1.5$

To gain further insight in phase locking we ran a measurement with a driving period of 1.5 and an amplitude of $A = 0.5$. The result is given in Fig. 5.7. Peaks of turbidity are located in intervals of ξ_{min} similar to previous findings. On the other hand every second interval is skipped. Thus we get a 2:1 phase locking.
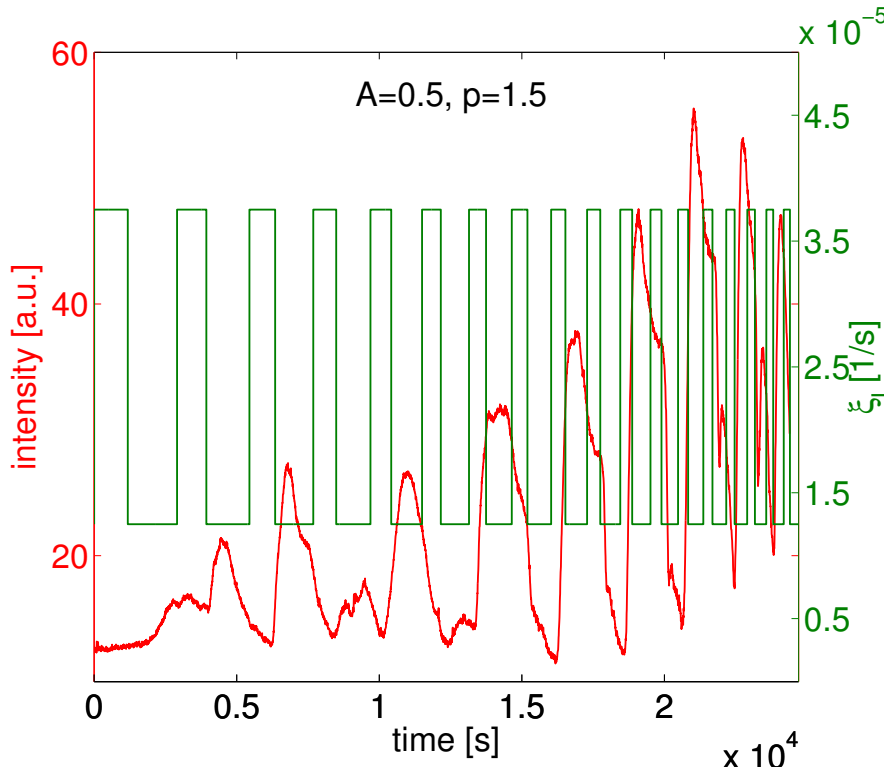
Figure 5.7: Measured 2:1 phase locking for a driving period of 1.5 and a high amplitude.

5.3.2 Driving Period $p = 0.5$

The result of another measurement is shown in Fig. 5.8. Here again an amplitude of $A = 0.5$ was choosen and the driving period was set to $p = 0.5$. Surprisingly, we find a 1:1 synchronization although we would rather expect a 1:2 locking. Furthermore, one observes that turbidity peaks are located within the ξ_{max} intervals which is different from what we have seen so far! If one brings to mind Fig. 5.1 it can be concluded that there has to be a transition from a 1:2 phase locking for small amplitudes to a 1:1 phase locking for high amplitudes.
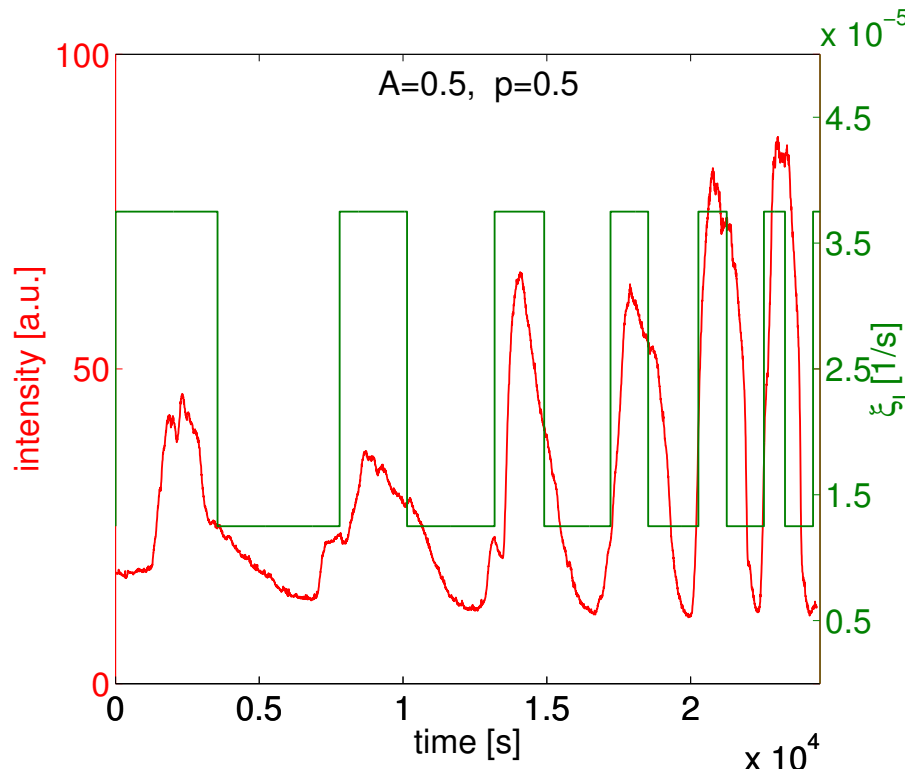
Figure 5.8: Measured 1:1 phase locking for a driving period of $p = 0.5$ and a high amplitude. Note that peaks of turbidity are located within intervals of ξ_{max} driving.

5.3.3 Driving Period $p \gg 1$

Until now we studied the case of driving periods that are in the same order of magnitude as the precipitation period. In Sec. 5.2.4 we showed that the observed phase locking can be described with the model of Sec. 2.2.2. However it is unlikely that this is a suitable description of the conditions in a real cloud. There we expect convective flows on smaller time scales than the precipitation period. Thus we address measurements with a driving period of $p = 5$ in this section.
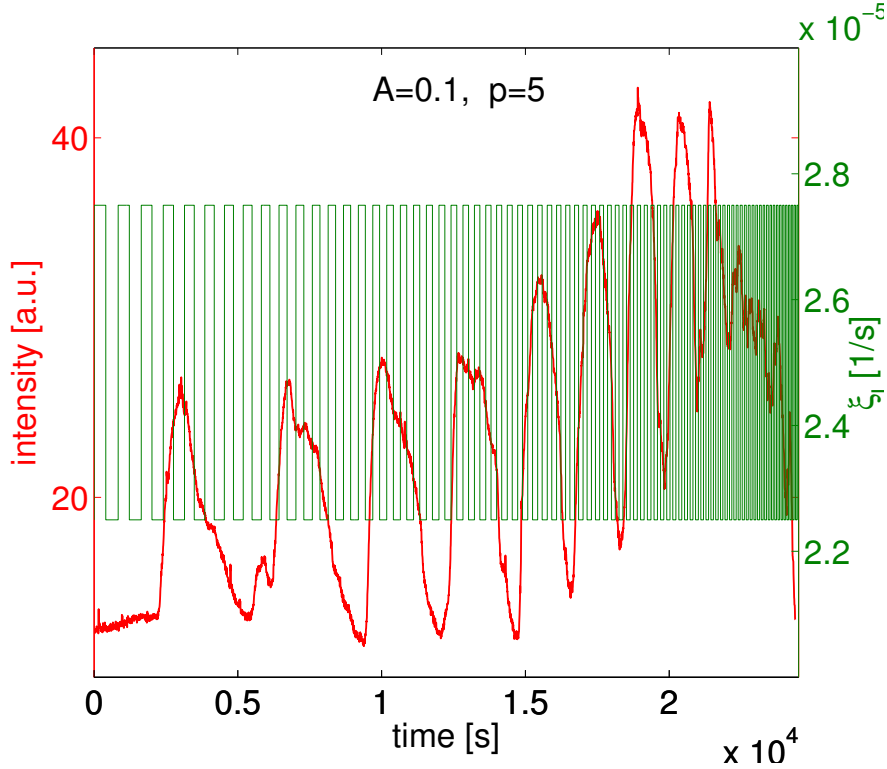
Figure 5.9: Turbidity for a fast oscillating driving ($p = 5$) and amplitude $A = 0.1$. Turbidity evolution is not much affected by the oscillations in the driving rate.

Fig. 5.9 shows the turbidity evolution for an amplitude of $A = 0.1$. We could not distinguish a big influence on the precipitation period from the turbidity measurement. It seems that for high driving frequencies there is an effect of averaging. To verify this statement we plotted the measured turbidity period Δt for two different amplitudes and a driving period of $p = 5$ in Fig. 5.10. It is compared to data we got from temperature ramps with a constant driving parameter that is consistent with the average ξ for the time-dependent heating. Additionally the prediction for a constant ξ is given. Data from time-dependent driving do not differ from the constant driving

but lie well within the fluctuations of Δt for constant driving. Thus, we conclude that the effect of ξ oscillations on the precipitation period is indeed negligible. Still there might be an influence on the microscale droplet distribution which can not be detected in turbidity measurement but requires a more complex setup.

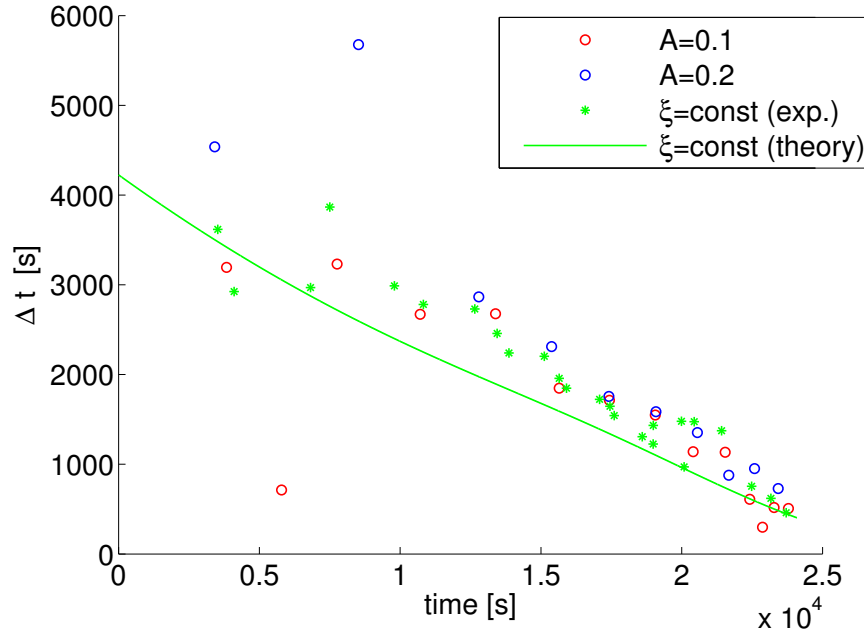**Figure 5.10:** Measured oscillation period Δt for time-dependent driving with driving period $p = 5$. Data for two different amplitudes are compared to Δt for a constant driving (green stars: measured data, green line: theoretical prediction).

6 Conclusions

We used a binary fluid of iso-butoxyethanol and water as a model system to study oscillations in precipitation. Previous experiments [2, 8, 9, 15] were run under idealized conditions, in particular by implementing a constant thermodynamic driving. We modified these experiments in two ways to gain insight into the validity of this idealization for the application to formation of warm rain in the atmosphere: The influence of moderate stirring was studied by inserting a small magnetic stirrer in the sample, and circulation in uprising clouds was modeled by exploring the consequences of oscillations in the driving parameter ξ. I developed temperature ramps for the oscillatory driving and modified the data analysis to illustrate phase locking (cf. Fig. 5.3).

6.1 Discussion

In the stirring experiments it is shown that stirring has an influence in the sense that oscillations in precipitation are suppressed for early times. Instead, we observe a continuous increase in turbidity with oscillations in the end. Regarding the period of oscillations we do not see a discrepancy to measurements without stirring.

The time-dependent driving is implemented by using a square wave function for the driving parameter ξ. Our data suggest that in the limit of high ξ frequencies the driving is dominated by the average value of ξ. Within our experimental errors the turbidity oscillation periods for a fast oscillatory driving are not different from those obtained with a constant driving.

On the other hand we find a rich variation of synchronization for driving frequencies that are close to the precipitation frequency. This includes the trivial case of a 1:1 phase locking for a 1:1 driving ($p = 1$). It was analysed for different amplitudes in the driving oscillations. We also give a qualitative explanation for the observation that minima of turbidity appear within regions of strong driving.

For lower amplitudes of ξ the phase locking is less pronounced and phase slips occure. To date we only looked at a few points in the parameter space as each measurement takes several hours. In many experiments we observe a phase locking over a few periods but not throughout the temperature ramp. As the number of oscillation in our experiments is limited it is sometimes not clear whether synchronization is given or not. Still, we obtained promising results and established a basis for future investigation.

6.2 Outlook

It was already mentioned that the collecting of data takes a lot of time and we therefore could only measure a few points in the parameter space of A and p. So far we have detected 1:1 and 2:1 phase locking, but at this point little can be said about the actual shape of the assumed Arnold tongues for synchronization. We know that there has to be a transition from 1:2 to 1:1 phase locking for a driving period of $p = 0.5$, but we could not yet specify for what amplitude the transition appears. For future investigations it might be valuable to scan a larger region in the parameter space and distinguish individual Arnold tongues. Eq. (5.1) could be used to examine the phase locking analytically. Furthermore it is reasonable to expand the analysis of fast oscillatory driving ($p \gg 1$), as this is assumed to be a good model for cloud convection. Only two different amplitudes were tested for this scenario.

For our experiments we used turbidity as a criterium for precipitation. It is not possible though to gain the droplet size distribution from turbidity. Further insights into the microphysics of the system could be obtained by a particle tracking method that has been developed by Lapp et al. [9]. It might be a worthwile approach to utilize synchronized oscillations for the matching of turbidity and droplet size distribution.

Appendix

Material Constants of Iso-Butoxyethanol and Water

The data for material constants have been collected and measured by T. Lapp, M. Rohloff, M. Wilkinson and J. Vollmer. This is unpublished work and therefore reproduced below.

The index $i \in \{\text{IBE}, \text{W}\}$ will be used to refer to material properties of IBE and water, respectively, and in accordance with the phase diagram 2.1 the concentration are always given in terms of $\phi = \phi_{\text{IBE}}$.

Density (based on Doi et al. [5])

The densities of the phases are determined by the composition, thermal expansion and molar excess volume,

$$\rho(\phi^m, T) = \left[\frac{\phi^m}{\rho_{\text{IBE}}} + \frac{(1 - \phi^m)}{\rho_{\text{W}}} + \left(\frac{\phi^m}{M_{\text{IBE}}} + \frac{(1 - \phi^m)}{M_{\text{W}}} \right) V_{\text{E}}^n \right]^{-1}. \tag{.1}$$

where $\rho_i = \rho_i(T)$ are the (temperature-dependent) densities of the pure substances, M_i their molar masses, and $V_{\text{E}}^n = V_{\text{E}}^n(\phi^n)$ is the molar excess volume.

The molar masses, M_i are $18.01528 \, \text{g/mol}$ for water[13] and $118.17416 \, \text{g/mol}$ for IBE[12], respectively.

The temperature dependence of the density, $\rho_i(T)$, of the pure substances is linearly approximated around $T_0 = 25°\text{C}$,

$$\rho_i(T) = \rho_i(T_0) - \alpha_i \cdot (T - T_0) \tag{.2}$$

with fit parameters for ρ_i and α_i given in table .1.

	$\rho_i(T_0)$ [g cm^{-3}]	α_i [g cm^{-3} K^{-1}]
water	0.997043	0.2571×10^{-3}
IBE	0.886255	0.968×10^{-3}

Table .1: Densities and thermal expansion coefficients for water and IBE [according to 5].

Moreover, the molar excess volume is fitted like [5]:

$$V_{\mathrm{E}}^n(\phi^n) \;=\; \frac{\phi^n \, (1 - \phi^n)}{1 - G \, \tilde{\phi}} \cdot \left(A_1 + A_2 \, \tilde{\phi} + A_3 \, \tilde{\phi}^2 \right) \tag{.3}$$

$$\text{with} \quad \tilde{\phi} \;=\; 1 - 2\phi^n$$

$$\text{and} \quad G \;=\; 0.975\,,$$

$$A_1 \;=\; -3.079 \ \mathrm{cm}^3/\mathrm{mol}\,,$$

$$A_2 \;=\; 1.801 \ \mathrm{cm}^3/\mathrm{mol}\,,$$

$$A_3 \;=\; 0.839 \ \mathrm{cm}^3/\mathrm{mol}\,.$$

A slight temperature dependence of these fit parameters was reported by [5]. However, it is so small that we need not take it into account here.

To get the dependence of the density difference on the reduced temperature the dependence $\phi(\theta)$ (coexistance curve) has to be inserted into equation .1.

Viscosity (own measurements augmented by data of Weast [22] and Menzel et al. [10])

We first provide the data of the pure phases, and then obtain the viscosity of the mixture by appropriate interpolation.

The viscosity of IBE was measured with an Ubbelohde viscosimeter type 537 10/I made by Schott. The temperature dependence of the viscosity η is fitted by

$$\eta_i(T) = A_i \times 10^{\frac{B_i \cdot (T_0 - T) - C_i \cdot (T_0 - T)^2}{T + D_i}} \tag{.4}$$

with $T_0 = 20°$ C and coefficients given in table .2. The values for water are taken from [22].

	A [kg m^{-1} s^{-1}]	B	C [(° C)$^{-1}$]	D [° C]
water	1.002×10^{-3}	1.3272	0.001053	105
IBE	3.36×10^{-3}	1.730	0.001	108

Table .2: Fit coefficients for the viscosity of water and IBE, defined by equation (.4), the data is taken from [22].

To interpolate the viscosities for a mixed phase of given mass fraction ϕ^m we use the composition-dependent viscosities at 25°C for a homogeneous mixture in the

single-phase regime, as provided by Menzel et al. [10]. The data is fitted with a fifth order polynomial

$$\eta(\phi^m, T = 25°C) = -40.66\,(\phi^m)^5 + 103.44\,(\phi^m)^4 - 100.32\,(\phi^m)^3$$
$$+ 39.35\,(\phi^m)^2 + 0.17\,\phi^m + 0.91. \tag{.5}$$

Assuming that the coefficients of interpolation are not changing substantially in the temperature range of our measurements, a rescaled viscosity $\tilde{\eta}(\phi^m)$ is defined. It only depends on the composition ϕ^m

$$\eta(\phi^m, T) = \tilde{\eta}(\phi^m) \cdot \eta_{\text{IBE}}(T) + [1 - \tilde{\eta}(\phi^m)] \cdot \eta_{\text{W}}(T). \tag{.6}$$

To check the strong assumption entering this interpolation, we also measured the viscosity of the two phases at $T = 40°C$. For both phases the prediction of viscosity3 was accurate to within 2%. This is sufficient for our means.

Diffusion coefficient (based on Steinhoff and Woermann [17])

Steinhoff and Woermann [17] provide only data on the diffusion coefficient. The renormalisation group theory predicts that the diffusion coefficient vanishes when the critical point is approached. On the other hand mode-coupling theory separates the diffusion coefficient into a backround and a singular part. According to Sengers [16] this has to be considered for the interpretation of experimental data. Since the used temperatures are outside the critical region for the coexistence curve, we expect not to see a critical exponent. Hence we fitted the data of Steinhoff and Woermann [17] with the following expression:

$$D_i(\theta) = D_c + \delta_i\,\theta \tag{.7}$$

with $D_c = 6.4 \times 10^{-12}\text{m}^2/\text{s}$, $\delta_{\text{IBE}} = 2.1 \times 10^{-9}\text{m}^2/\text{s}$ and $\delta_{\text{W}} = 4.1 \times 10^{-9}\text{m}^2/\text{s}$.

Interfacial tension (based on Aratono et al. [1])

The interfacial tension vanishes at the critical temperature, and its dependence at higher temperatures can be represented by a power law

$$\gamma(\theta) = \gamma_0 \cdot \theta^{\alpha_\gamma}. \tag{.8}$$

where a fit to the data of [1] yields $\gamma_0 = 7.3 \times 10^{-4}$N/m and $\alpha_\gamma = 1.2$.

Molar volume (based on Douheret et al. [6])

According to [6] the molar volume V^n can be approximated by

$$V^n = \phi^n\, V^n_{\text{IBE}} + (1 - \phi^n)\, V^n_{\text{W}} \tag{.9}$$

with $V^n_{\text{IBE}} = 124\text{cm}^3/\text{mol}$ and $V^n_{\text{W}} = 15.98\text{cm}^3/\text{mol}$.

Bibliography

[1] M. Aratono, S. Nakayama, N. Ikeda, and K. Motomura. Thermodynamic consideration on the interface formation of water and ethylene glycol isobutyl ether mixture. *Colloid Polym. Sci.*, 268:877–882, 1990.

[2] G. K. Auernhammer, D. Vollmer, and J. Vollmer. Oscillatory instabilities in phase separation of binary mixtures: Fixing the thermodynamic driving. *J. Chem. Phys.*, 123:134511, 2005.

[3] I. J. Benczik and J. Vollmer. A reactive-flow model of phase separation in fluid binary mixtures with continuously ramped temperature. *Europhys. Lett.*, 91:36 003, 2010.

[4] M. E. Cates, J. Vollmer, A. Wagner, and D. Vollmer. Phase separation in binary fluid mixtures with continuously ramped temperature. *Phil. Trans. R. Soc. Lond. A*, 361:793–807, 2003.

[5] H. Doi, K. Tamura, and S. Murakami. Thermodynamic properties of aqueous solution of 2-isobutoxyethanol at T=(293.15, 298.15, and 303.15) K, below and above LCST. *J. Chem. Thermodyn.*, 32:729–741, 2000.

[6] G. Douheret, M. I. Davis, J. C. R. Reis, I. J. Fjellanger, M. B. Vaage, and H. Hoiland. Aggregative processes in aqueous solutions of isomeric 2-butoxyethanols at 298.15 K. *Phys. Chem. Chem. Phys.*, 4:6034–6042, 2002.

[7] R. A. Houze Jr. *Cloud Dynamics*, volume 53 of *International Geophysics*. Academic Press, 1993.

[8] T. Lapp. *Evolution of droplet distributions in hydrodynamic systems.* PhD thesis, Georg-August-Universität Göttingen, 2011.

[9] T. Lapp, M. Rohloff, J. Vollmer, and B. Hof. Particle tracking for polydisperse sedimenting droplets in phase separation. *Exp. Fluids*, 52:1187–1200, 2012.

Bibliography

[10] K. Menzel, S. Z. Mirzaev, and U. Kaatze. Crossover behavior in micellar solutions with lower critical demixing point: Broadband ultrasonic spectrometry of the isobutoxyethanol-water system. *Phys. Rev. E*, 68:011501, 2003.

[11] A. Pikovsky, M. Rosenblum, and J. Kurths. *Synchronization - a universal concept in nonlinear science*, volume 12 of *Cambridge Nonlinear Science Seriese*. Cambridge University Press, 2001.

[12] National Center for Biotechnology Information PubChem. Pubchem compound database, July 17 2013. URL `http://pubchem.ncbi.nlm.nih.gov/summary/summary.cgi?cid=521158`. CID=521158 (17 July 2013).

[13] National Center for Biotechnology Information PubChem. Pubchem compound database, July 17 2013. URL `http://pubchem.ncbi.nlm.nih.gov/summary/summary.cgi?cid=962`. CID=962 (17 July 2013).

[14] W. Roedel. *Physik unserer Umwelt: die Atmosphäre.* Springer Berlin Heidelberg, 2000.

[15] M. Rohloff. Measuring the droplet-size and velocity distributions in binary phase separation. Diploma thesis, Georg-August-Universität Göttingen, 2011.

[16] J. V. Sengers. Transport properties of fluids near critical points. *Int. J. Thermophys.*, 6:2003–232, 1985.

[17] B. Steinhoff and D. Woermann. Slowing down of the kinetics of liquid/liquid phase separation along the binodal curve of a binary liquid mixture with a miscibility gap approaching the critical point. *J. Chem. Phys.*, 103:8985–8992, 1995.

[18] S. N. Timasheff. Turbidity as a criterion of coagulation. *J. Colloid Interface Sci.*, 21:489–497, 1966.

[19] D. Vollmer, R. Strey, and J. Vollmer. Oscillating phase separation in microemulsions. I. experimental observation. *J. Chem. Phys.*, 107:3619–3626, 1997.

[20] D. Vollmer, J. Vollmer, and A. J. Wagner. Oscillatory kinetics of phase separation in a binary mixture under constant heating. *Phys. Chem. Chem. Phys.*, 4:1380–1385, 2002.

[21] J. Vollmer, G. K. Auernhammer, and D. Vollmer. Minimal model for phase separation under slow cooling. *PRL*, 98:115701, 2007.

[22] R. C. Weast. *CRC Handbook of Chemistry and Physics.* CRC Press, Inc. Boca Raton, Florida, 69. edition, 1988-1989.

Erklärung nach §13(8) der Prüfungsordnung für den Bachelor-Studiengang Physik und den Master-Studiengang Physik an der Universität Göttingen:

Hiermit erkläre ich, dass ich diese Abschlussarbeit selbständig verfasst habe, keine anderen als die angegebenen Quellen und Hilfsmittel benutzt habe und alle Stellen, die wörtlich oder sinngemäß aus veröffentlichten Schriften entnommen wurden, als solche kenntlich gemacht habe.

Darüberhinaus erkläre ich, dass diese Abschlussarbeit nicht, auch nicht auszugsweise, im Rahmen einer nichtbestandenen Prüfung an dieser oder einer anderen Hochschule eingereicht wurde.

Göttingen, den August 15, 2013

(Julian Vogel)